

# Pressure Triggers Structural Phase Transitions in Chiral $\text{ErFe}_3(\text{BO}_3)_4$

Yanhong Gu,<sup>‡</sup> Fan Yang,<sup>‡</sup> Choongjae Won, Sang-Wook Cheong, Turan Birol, and Janice L. Musfeldt\*



Cite This: *J. Phys. Chem. C* 2026, 130, 1248–1256



Read Online

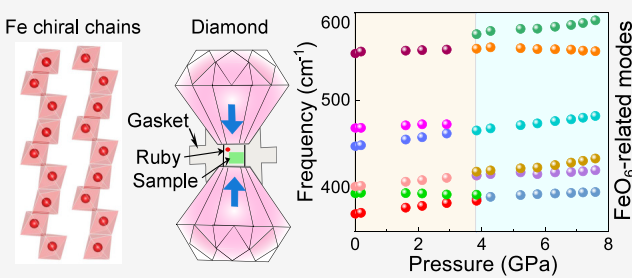
ACCESS |

Metrics & More

Article Recommendations

Supporting Information

**ABSTRACT:** We combined diamond anvil cell techniques with Raman scattering and near-infrared spectroscopies plus lattice dynamics calculations and a symmetry analysis to reveal the properties of  $\text{ErFe}_3(\text{BO}_3)_4$  under compression. Overall, the system is surprisingly soft, with a series of structural phase transitions (but no metallicity) up to 20 GPa. Bringing frequency vs pressure trends together with a group–subgroup analysis and examination of the energy landscape, we uncover a structural phase transition from  $P3_121$  to either  $P321$  or  $R32$  across the 3.8 GPa transition. The  $\text{BO}_3^-$  units are robust, whereas the Fe helix is soft and flexible. Analysis of the crystal field excitations reveals that the local symmetry of  $\text{Er}^{3+}$  remains trigonal prismatic until after 8.6 GPa with significantly lower symmetries realized at higher pressures. Evaluation of spin–phonon coupling across the 40 K magnetic ordering transition and spectral modifications through the 450 K structural phase transition place this material on a firm foundation, paving the way for a combination of external stimuli including magnetic field, pressure, and strain.



## INTRODUCTION

Chirality, the property of being unable to superimpose an object upon its mirror image, plays a pivotal role in chemistry, biology, medicine, and catalysis,<sup>1,2</sup> although the topic is underexplored in solids.<sup>3–5</sup> This is largely due to the limited number of monochiral materials, a lack of sensitivity to the requisite symmetry elements, and the need for improved theoretical frameworks able to predict their properties.<sup>5–10</sup> One platform of current interest is the borates with chemical formula  $\text{RM}_3(\text{BO}_3)_4$  ( $\text{R} = \text{La–Lu, Y}$ ;  $\text{M} = \text{Al, Ga, Cr, Fe, Sc}$ ). In these systems, chirality delivers both magnetoelectric coupling and fascinating magnetic behavior. Different combinations of  $\text{R}^{3+}$  and  $\text{M}^{2+}$  naturally lead to distinct magnetic configurations with spins ordering either in or out of the  $ab$  plane,<sup>11–15</sup> and rare earth size effects cause structural phase transitions at different temperatures.<sup>16–18</sup> The chemical nature of the metal and rare earth ions determines other properties as well. For instance, aluminum borates are widely used in lasing applications<sup>19,20</sup> whereas the iron borates host magnetoelectric coupling.<sup>21,22</sup> Many of the rare earth ferroborates  $\text{RFe}_3(\text{BO}_3)_4$  are noncentrosymmetric multiferroics with chiral crystal structures.  $\text{DyFe}_3(\text{BO}_3)_4$  hosts quadrupole helix chirality which leads to new functionalities including chiral optical activity and the possibility of low power electronics.<sup>23</sup> In these systems, directional anisotropy of the chiral Fe chain and single-ion anisotropy of the rare earth centers are the chief contributors to spin behavior.<sup>24,25</sup> Specifically, the Fe sublattice determines the antiferromagnetic ordering temperature (typically near 30 or 40 K). The interaction between rare earth ions is weak, so ordering occurs below 10 K.<sup>26</sup> Fe–Fe and Fe–R interactions are therefore key to understanding and

controlling the magnetic properties. Naturally, external stimuli like magnetic field are powerful tools for manipulating the properties of  $\text{RFe}_3(\text{BO}_3)_4$  materials.<sup>21,27–30</sup> Pressure is another well-known tuning parameter that acts directly on bond lengths and angles.<sup>31–35</sup> By so doing, it can modify properties like structure, spin orientation, and polarization<sup>36–38</sup> in a manner that is much cleaner than chemical substitution.<sup>39</sup>  $\text{GdFe}_3(\text{BO}_3)_4$ , for instance, displays a polar  $R3$  space group and ferroelectricity under pressure.<sup>40</sup>

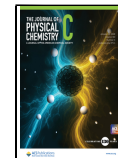
We selected  $\text{ErFe}_3(\text{BO}_3)_4$  as a platform for exploring the properties of a chiral mixed metal oxide under compression. The high temperature phase hosts an  $R32$  space group with  $\text{FeO}_6$  octahedra forming helical chains along the  $c$  axis [Figure 1a].<sup>41,42,44,45</sup> At the same time, trigonal prisms of  $\text{ErO}_6$  connect three helical  $\text{FeO}_6$  chains, although these building blocks remain isolated, with no  $\text{Er} \cdots \text{O} \cdots \text{Er}$  paths. Decreasing temperature drives an  $R32$  to  $P3_121$  structural phase transition [Figure 1b].<sup>16</sup> As part of this process, the Er site symmetry drops from  $D_3$  to  $C_2$ , and the overall number of nonequivalent positions increases. The  $\text{ErO}_6$  trigonal prisms and  $\text{FeO}_6$  octahedra also become increasingly distorted in the low temperature phase. Planar  $\text{BO}_3$  triangles connect the  $\text{FeO}_6$  octahedra and the  $\text{ErO}_6$  trigonal prisms. Their surfaces are roughly parallel to the  $ab$  plane depending on the type of

Received: November 9, 2025

Revised: December 26, 2025

Accepted: December 30, 2025

Published: January 7, 2026



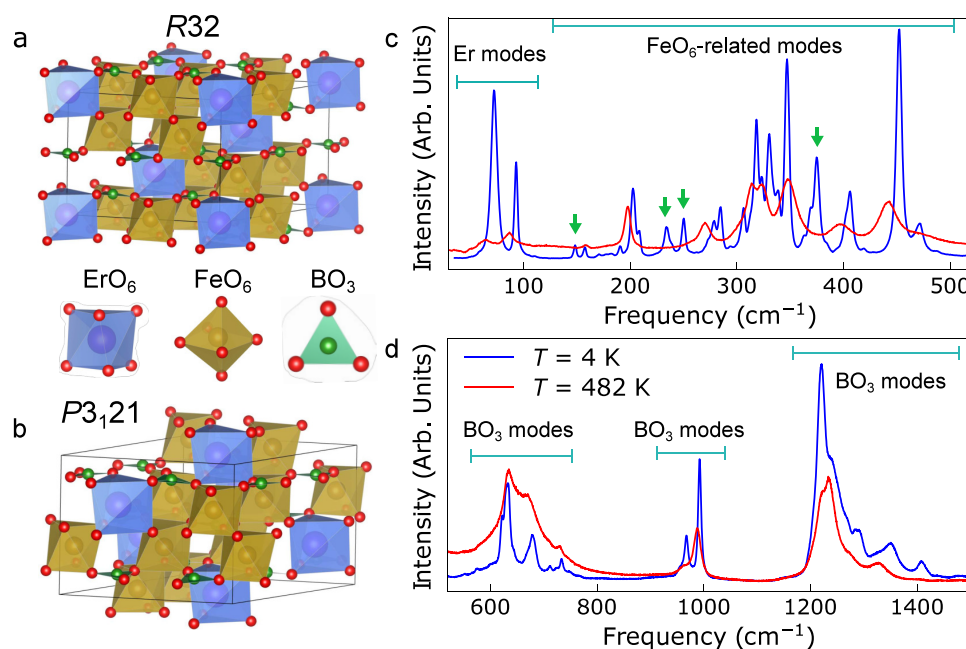


**Figure 1.** Crystal structures and Raman-active vibrational modes of  $\text{ErFe}_3(\text{BO}_3)_4$ . (a, b) Crystal structures in the  $R\bar{3}2$  and  $P\bar{3}_121$  space groups<sup>11,41–43</sup> corresponding to the high and low temperature phases, respectively, along with an illustration of the  $\text{ErO}_6$ ,  $\text{FeO}_6$ , and  $\text{BO}_3$  building blocks. There are both equilateral and isosceles  $\text{BO}_3$  units. (c, d) Raman-active modes of  $\text{ErFe}_3(\text{BO}_3)_4$  in the  $P\bar{3}_121$  (4 K) and  $R\bar{3}2$  (482 K) space groups, collected on a single crystal with a random orientation. These features are assigned based upon our lattice dynamics calculations which reveal a clear separation of energy scales and a strong clustering of related motions. Green arrows indicate new modes that appear in the low temperature phase.

triangle (equilateral or isosceles) in both the high and the low temperature phases. Ordering of the Fe magnetic moments takes place near 40 K, whereas Er moments order at approximately 10 K.<sup>11</sup> Based upon the 32.1' maximal low temperature point group<sup>11,46</sup> and the fact that neighboring unit cells along the  $c$  axis reportedly have exactly opposite spin patterns, the magnetic structure of  $\text{ErFe}_3(\text{BO}_3)_4$  is antiferromagnetic. However, since the crystal structure in the paramagnetic phase is chiral to begin with, the lack of an altermagnetic spin splitting is due to the presence of antitranslation (translation followed by time-reversal) only, and any subtle change in crystal structure or spin directions, including any helical character that can be easily induced on the already noncollinear spin structure, is likely to induce altermagnetic spin splittings in this compound.

In this work, we combine diamond anvil cell techniques with Raman scattering and near-infrared absorption spectroscopy to unravel a series of pressure-driven structural phase transitions in  $\text{ErFe}_3(\text{BO}_3)_4$ . Comparison with complementary lattice dynamics calculations allows us to assign the character of various phonons in this system at ambient conditions, and a focus on the first of a total of four compression-induced transitions along with a correlation group analysis and survey of the energy landscape reveals a change in the space group from  $P\bar{3}_121$  to either  $P\bar{3}21$  or  $R\bar{3}2$  at 3.8 GPa. Remarkably, the modes involving Fe centers in the chiral chain exhibit the most significant changes, while phonons related to the  $\text{BO}_3$  triangles and  $\text{ErO}_6$  octahedra harden systematically. We conclude that the chiral arrangement of Fe centers is relatively soft and flexible, whereas the  $\text{BO}_3$  and  $\text{ErO}_6$  environments are more rigid. In line with these findings, the rare earth  ${}^4\text{I}_{15/2} \rightarrow {}^4\text{I}_{13/2}$  crystal field excitations display only slight frequency shifts under compression up to approximately 8 GPa, suggesting that the local trigonal prismatic symmetry of  $\text{Er}^{3+}$  remains almost

unchanged from that under ambient conditions. Systematic temperature studies, on the other hand, reveal low frequency Er-containing phonons with strong precursor effects on approach to the 450 K structural phase transition. These precursor effects coordinate with well-defined jumps of selected  $\text{FeO}_6$ - and  $\text{BO}_3$ -related modes to lower frequencies at the transition itself. The spin–phonon coupling constants that we extract across the 40 K magnetic ordering transition are essentially zero. Taken together, our findings demonstrate that tunability in iron borates can be extended beyond magnetic field<sup>47,48</sup> to include both pressure and temperature effects.

## METHODS

### Crystal Growth and Diamond Anvil Cell Loading

High quality single crystals of  $\text{ErFe}_3(\text{BO}_3)_4$  were grown by flux techniques as described previously.<sup>49</sup> These crystals are monochiral, meaning that there are no chiral domains. For the high pressure Raman scattering measurements, a small single crystal was loaded into a symmetric diamond anvil cell suitable for work in the 0–20 GPa range. The cell is equipped with low fluorescence diamonds and 400  $\mu\text{m}$  culets. We also employed a stainless steel gasket with a 100  $\mu\text{m}$  hole, KBr as the pressure medium to ensure quasi-hydrostatic conditions, and an annealed ruby ball for pressure determination via fluorescence.<sup>50</sup> Ruby fluorescence spectra are shown in Figure S1, Supporting Information. For high pressure near-infrared measurements, no pressure medium is used; only pure samples and a ruby ball are loaded into the diamond anvil cell. Additional information on hydrostaticity and reversibility is available in Figure S2, Supporting Information.

### Raman Scattering Spectroscopy

Raman scattering measurements were performed in the back scattering geometry using a Horiba LabRAM HR Evolution spectrometer equipped with a 532 nm (green) laser, a 50×

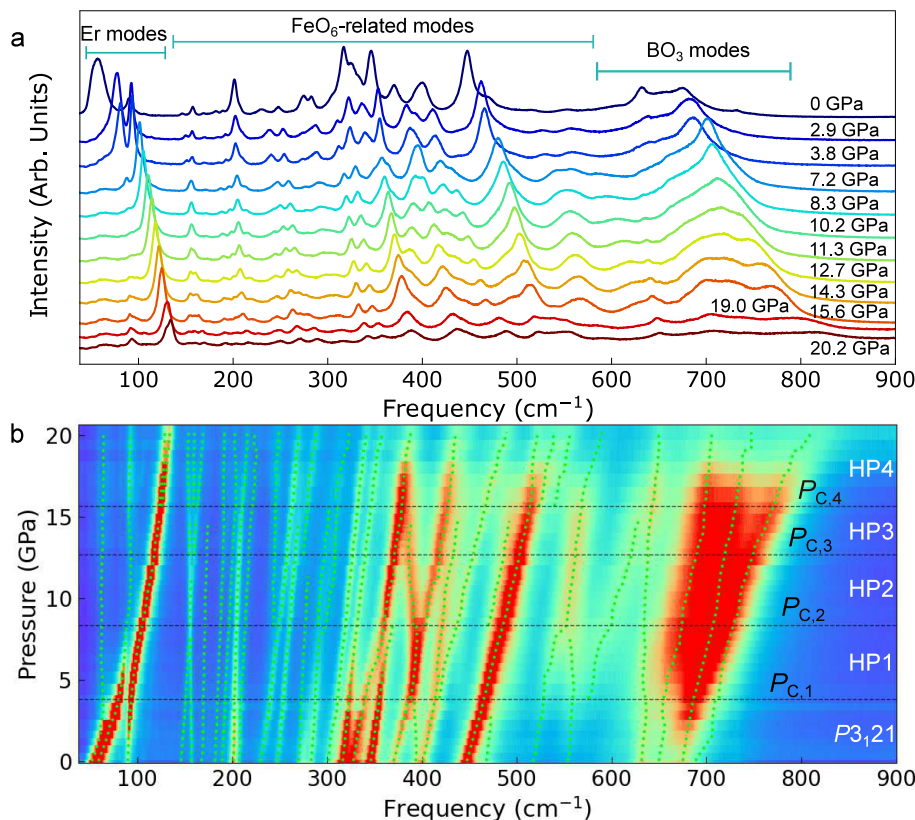


**Figure 2.** Raman scattering response under pressure. (a) Raman scattering response of  $\text{ErFe}_3(\text{BO}_3)_4$  under compression from 0 (top, dark blue) to 20.2 GPa (bottom, dark red) at room temperature. These spectra are reversible upon release of the pressure up to 20 GPa. (b) Contour plot of the Raman spectra as a function of pressure. In addition to the ambient pressure phase, four new states are induced by pressure and marked by the horizontal dashed lines. They are labeled HP1, HP2, HP3, and HP4. A close-up view of panel b is shown in Figure S3, Supporting Information.

microscope objective, 1800 line/mm gratings, and a liquid-nitrogen-cooled charge-coupled device detector. To minimize heating and maximize signal intensity for this low brightness sample, the power was controlled below 2 mW, and the laser was slightly defocused. Each spectrum was integrated for 40 s and averaged three times. Variable temperature work was carried out with a low-profile open-flow cryostat, and high pressure measurements employed a diamond anvil cell, as described above. Standard peak fitting techniques were employed, as appropriate.

#### Near-Infrared Spectroscopy

Near-infrared spectra are collected in transmittance mode using a Bruker Equinox 55 FTIR spectrometer with a Bruker IR Scope II. A tungsten source and a liquid N<sub>2</sub>-cooled InSb detector are used in the frequency range of 4000–12000 cm<sup>-1</sup>. Spectra were obtained from the sample loaded in the diamond anvil cell at a resolution of 4 cm<sup>-1</sup> at room temperature.

#### First-Principles Structural Relaxation and Phonon Analysis

First-principles calculations were performed using density functional theory (DFT)<sup>51</sup> as implemented in Vienna *ab initio* simulation package with projector augmented wave (PAW) method and Perdew–Burke–Ernzerhof (PBE) exchange–correlation functional<sup>52</sup> revised for solids (PBEsol),<sup>53</sup> which is empirically known to be reliable in reproducing crystal structures in solid bulk systems.<sup>54</sup> 4f electrons in erbium atoms are included in the core, as we do not consider the magnetic moments on the Er sites. On-site interelectron repulsion of  $U = 2$  eV and Hund's coupling  $J = 0.7$  eV are added for 3d electrons of iron, and it is observed that the system is not sensitive to the choice of  $U$  values (see Supporting Information). Cut-off energy is set as 500 eV. Electronic convergence threshold for self-consistent loop is set to be  $10^{-4}$  meV ( $10^{-3}$  meV) per ferromagnetic (antiferromagnetic) cell; break condition of structural relaxation is set

to be  $10^{-2}$  meV ( $10^{-1}$  meV) per ferromagnetic (antiferromagnetic) cell. Phonon modes are obtained using finite displacement method. Spin–orbit coupling is not considered. Additional information is available in Supporting Information.

## RESULTS AND DISCUSSION

### Raman Scattering Response of $\text{ErFe}_3(\text{BO}_3)_4$ and Vibrational Mode Assignments

Figure 1 displays the Raman scattering response of  $\text{ErFe}_3(\text{BO}_3)_4$  in the high and low temperature phases. These spectra were collected on the random surface of the single crystal to reveal as many peaks as possible. The space group in the high temperature phase is R32 whereas that in the low temperature phase is P3<sub>1</sub>21.<sup>16,42,55,56</sup> A group theoretical analysis has been presented in prior work.<sup>16</sup> As a reminder, the primitive cell of the R32 structure contains 20 atoms, which gives rise to 57 vibrational modes including 12 infrared-active and 45 Raman-active features. The low temperature primitive cell of the P3<sub>1</sub>21 structure contains 60 atoms, resulting in 32 infrared-active and 145 Raman-active modes. Clearly this is a complicated situation. To support these measurements, we performed lattice dynamics calculations to reveal the mode displacement patterns. Even so, it is challenging to make unambiguous mode assignments with so many features in close proximity. We therefore assign the excitations as consistently as possible based upon the mode groupings. The approach works because there is a clear separation of energy scales and “clustering” of the various types of vibrations. This allows us to classify the general character of the motion. For instance,

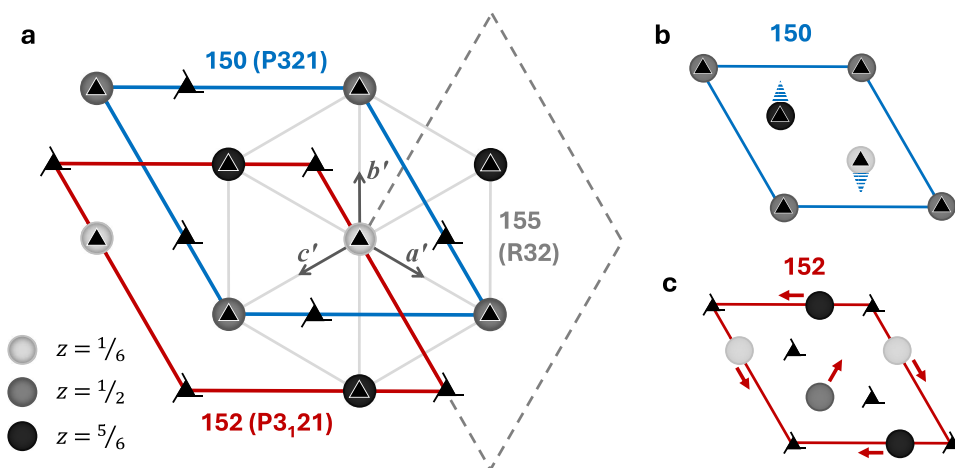


**Figure 3.** Symmetry relationship among space groups  $P321$  (No. 150),  $R32$  (No. 155) and  $P3_21$  (No. 152). (a) Unit cells of  $P321$  (blue) and  $P3_21$  (red) superimposed on the  $R32$  unit cells, primitive (solid gray lines) and conventional (dashed gray lines).  $C_3$  rotational axes and  $3_1$  screw axes in  $R32$  are labeled with corresponding symmetry symbols (with  $3_2$  axes and  $C_2$  axes omitted for simplicity). Gray balls with different shade levels represent Er atoms at different  $z$ -levels. (b, c) Boundary phonon modes in No. 155 that lead to No. 150 and No. 152, respectively. Shaded triangles represent out-of-plane displacements; solid arrows represent in-plane displacements.

according to the phonon density of states from our density functional theory (DFT) calculations, the lowest frequency peaks are clearly due to Er vibrations, whereas  $FeO_6$  motion resides between approximately 200 and 500  $cm^{-1}$ . The borate units<sup>16,57–59</sup> have well-known features near 650, 980, and 1220  $cm^{-1}$ . These assignments are discussed in detail in the *Supporting Information*. The other interesting aspect of Figure 1c,d is that several of the Raman-active modes in the 4.2 K spectrum disappear in the high temperature phase. These features, all below 400  $cm^{-1}$ , are marked with green arrows. A more detailed discussion of the temperature dependence of these features across the magnetic and structural phase transitions is given below.

#### Pressure Triggers a Series of Structural Phase Transitions

Figure 2a summarizes the Raman scattering response of  $ErFe_3(BO_3)_4$  as a function of the pressure between 0 and 20 GPa. The pressure vs frequency trends (plotted as green circles) are shown in Figure 2b. Here, color represents mode intensity. As usual, we define the critical pressures ( $P_C$ 's) from an analysis of the peak splitting, shifting, and recombination under compression.<sup>60,61</sup> These changes can be connected with symmetry breaking and restoration through correlation group analysis. We find four structural phase transitions in  $ErFe_3(BO_3)_4$  ( $P_{C,1} = 3.8$ ,  $P_{C,2} = 8.3$ ,  $P_{C,3} = 12.7$ ,  $P_{C,4} = 15.6$  GPa) as indicated by the horizontal dashed lines in Figure 2b. In addition to the  $P3_21$  state at ambient pressure, the critical pressures define four new structural phases, marked as HP1, HP2, HP3, and HP4. In order to focus our attention, we concentrate on unraveling the symmetry properties across  $P_{C,1} = 3.8$  GPa. A similar distortion is likely to be triggered by small strains, as well.

The ambient pressure  $P3_21$  space group (No. 152) hosts  $Er^{3+}$  ions with  $C_2$  site symmetry and  $Fe^{2+}$  ions with both  $C_2$  and  $C_1$  site symmetries. The Fe framework forms a 3-fold screw axis, whereas the Er centers host 2-fold rotational symmetry. Examination reveals that the peaks at 400 and 470  $cm^{-1}$  disappear across the structural phase transition at 3.8 GPa. At the same time, two new features appear near 430 and 570  $cm^{-1}$ . These are iron oxide bending motions. The number of low frequency Er-containing modes below 100  $cm^{-1}$  as well as

the overall quantity of high frequency borate-related modes remain similar. We can immediately see that the borate framework is quite robust under compression, so the symmetry elements that these phonons represent are unchanged. The helical iron oxide framework is significantly softer.

#### Symmetry and Energy Landscape Analysis in $ErFe_3(BO_3)_4$ under Pressure

Based upon the overall number of phonon modes in the Raman scattering spectrum across  $P_{C,1}$ , the new high pressure phase of  $ErFe_3(BO_3)_4$  (which we label as HP1) should contain a similar number of atoms in the primitive cell. A symmetry analysis<sup>62–64</sup> yields five candidate space groups:  $P321$  (No. 150),  $P3_112$  (No. 151),  $P3_21$  (No. 154),  $P6_1$  (No. 169), and  $P6_4$  (No. 172). Crystals that form an enantiomorphous pair, i.e., a crystal and its mirror image with opposite chirality, have the same excitation spectrum. Hence, they exhibit the same peaks in the Raman spectrum.<sup>65,66</sup> The observed splitting and merging of modes in our spectra suggest that the transition from the ambient right-handed space group is not a simple flipping of handedness. Thus, the left-handed space group  $P3_21$  (No. 154) can be excluded from further analysis.  $P6_1$  (No. 169) contains only  $C_1$  site symmetry and, compared with the  $3_1$  screw, requires a helical Fe chain that has 6 planes of Fe atoms in each unit cell. As a result, this group requires at least a doubled unit cell with significant rearrangement of atoms and would yield many more peaks. It is therefore excluded from further consideration based on the overall number of site symmetries. For  $P6_4$  (No. 172), there is no in-plane 2-fold rotational symmetry axis, which contradicts the observation that the Er-related modes maintain their character in the HP1 phase. In other words, because the number of Er-related modes remains the same across  $P_{C,1}$ , it is likely that the in-plane 2-fold rotation symmetry is preserved at Er sites despite the frequency shift and change in intensity. A symmetry analysis of the spectroscopic results therefore suggests that the most likely candidates for HP1 are either  $P321$  (No. 150) or  $P3_112$  (No. 151).

To more deeply examine the possible structures across 3.8 GPa, we performed first-principles calculations by building candidate structures in space groups  $R32$  (No. 155),  $P321$

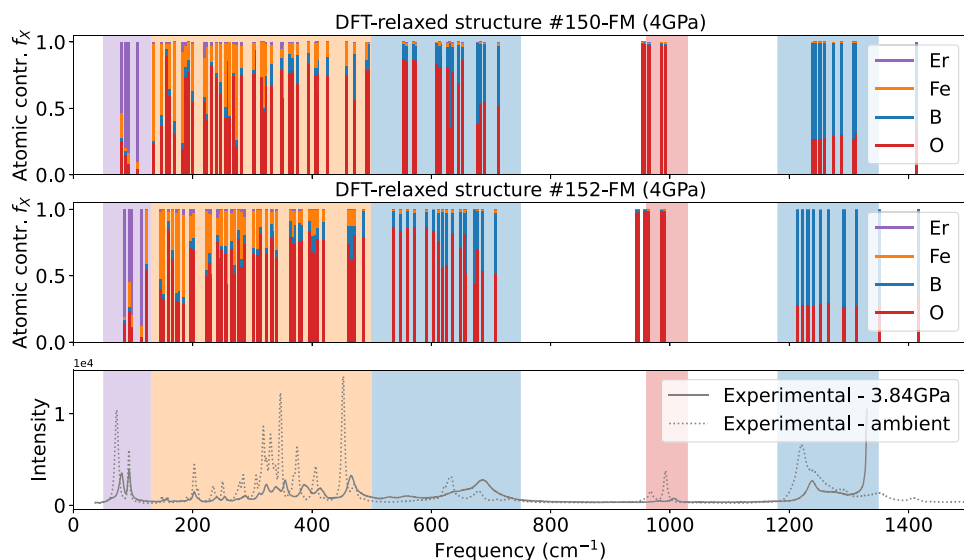


**Figure 4.** DFT-predicted Raman-active phonon modes and corresponding atomic contributions of ferromagnetic (FM)  $\text{ErFe}_3(\text{BO}_3)_4$  with space group No. 150 ( $P321$ ) and No. 152 ( $P3_121$ ) under 4 GPa. Shaded regions correspond to (purple)  $\text{ErO}_6$  modes, (orange)  $\text{FeO}_6$ -related modes, (blue)  $\text{BO}_3$  modes, and (red) O-dominant modes. Calculation details can be found in Supporting Information.

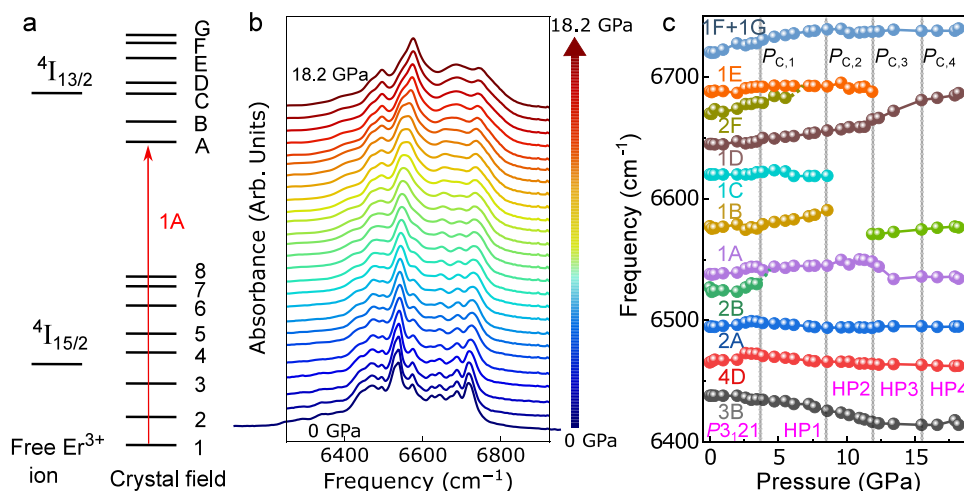


**Figure 5.**  $f$ -manifold excitations of  $\text{ErFe}_3(\text{BO}_3)_4$  under pressure. (a) Scheme showing the crystal field energy levels of an  $\text{Er}^{3+}$  ion. (b) Near infrared absorbance of  $\text{ErFe}_3(\text{BO}_3)_4$  at room temperature between 0 (bottom solid line) and 18.2 GPa (top solid line). (c)  $f$ -manifold excitations as a function of pressure. Peak 2B is very small and strongly overlaps peak 1A in this range, making it challenging to track in a meaningful way. These spectra are reversible upon the release of the pressure.

(No. 150), and  $P3_12$  (No. 151) in the ferromagnetic configuration, with primitive unit cells consisting of 20, 60, and 60 atoms, respectively. For space group  $P3_12$ , the only likely structure we can find with the same stoichiometry as  $\text{ErFe}_3(\text{BO}_3)_4$  stabilizes into a very different configuration where each B atom is coordinated by four O atoms,<sup>67</sup> leading to dramatic softening of  $\text{BO}_x$  phonon modes in high frequency region as illustrated in the Supporting Information. This ruled out  $P3_12$  as a candidate for HP1.  $P321$  and  $R32$  are both able to stabilize in structures similar to those of the ambient  $P3_12$  phase with only minor displacements in atomic positions. Symmetry analysis reveals that  $R32$  (No. 155) is a common supergroup of  $P321$  (No. 150) and  $P3_12$  (No. 152, the ambient phase). All three systems share very similar crystal structures with some transformation of unit cells, and  $P321$  and  $P3_12$  are accessible from  $R32$  through two different boundary phonon modes [Figure 3]. Energetically, DFT

predicts  $P3_12$  to be the most favorable phase throughout the pressure range from 0 to 4 GPa, followed by  $R32$  with a difference of approximately 200 meV in free energy per conventional unit cell (60 atoms), far exceeding the electronic convergence threshold of  $10^{-4}$  meV and the structural relaxation condition of  $10^{-2}$  meV. Although DFT apparently does not predict a phase transition, the metastable phases captured by it can nevertheless be used to provide some insight into possible high pressure structure candidates which are expected to be at similar energy levels as the ambient phase around the transition point.  $P321$  cannot be stabilized over  $R32$  in a ferromagnetic configuration and always relaxes into the higher-symmetry  $R32$  structure during the structural optimization process in DFT. However, we do not rule out the possibility that  $P321$  may be stable in other magnetic configurations. Regarding Raman spectra, our calculations confirm the same grouping of Raman-active phonon modes in

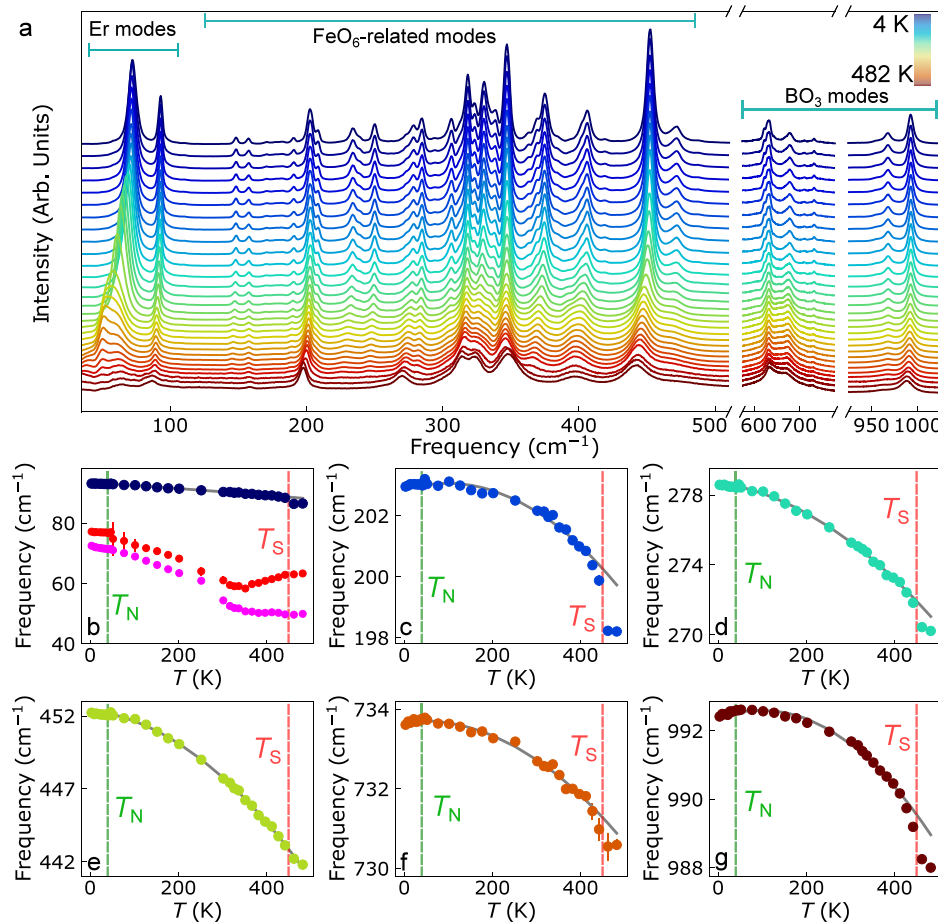


**Figure 6.** Temperature dependence of the Raman spectra. (a) Raman-active phonon modes at various temperatures. (b–g) Frequency vs temperature trends. Circles represent experimental data extracted from panel a, and solid gray lines are fits to the anharmonic model. Unless indicated, the error bars are smaller than the symbol size.

*P321* and *P3<sub>1</sub>21*, with observable differences in the frequency distribution between 300 and 600 cm<sup>-1</sup> [Figure 4]. *R32* has a much smaller primitive cell and thus many fewer Raman-active phonon modes; however, given the almost indistinguishable crystal structures of *R32* and *P321* obtained from our calculations, the zone boundary modes in *R32* which fold onto  $\Gamma$  and become visible in *P321* are expected to be very weak in intensity, leading to highly similar spectral patterns for the two candidates in practice. As a result, we maintain both *P321* (No. 150) and *R32* (No. 155) as possible candidates for the space group above 3.8 GPa.

#### Analysis of the Local Rare Earth Environment

To determine whether the local environment of the rare earth center varies across *P<sub>C,1</sub>*, we measured the near-infrared absorbance of ErFe<sub>3</sub>(BO<sub>3</sub>)<sub>4</sub> as a function of the pressure [Figure 5]. These features can be assigned as *f*-manifold excitations of Er<sup>3+</sup>. As expected, the positions of these crystal field excitations at ambient conditions are consistent with prior reports.<sup>55,68,69</sup> Figure 5c displays the frequency vs pressure trends. Importantly, there are no clear anomalies across the structural phase transition at *P<sub>C,1</sub>*. The overall lack of prominent changes in the *f*-manifold excitations suggests that Er<sup>3+</sup> remains in a trigonal prismatic environment across *P<sub>C,1</sub>* = 3.8 GPa. This supports a structural phase transition at *P<sub>C,1</sub>* that, from a chemical point of view, primarily involves the Fe helix. The local Er<sup>3+</sup> environment is more robust, consistent with our

analysis above. Finally, we point out that ErFe<sub>3</sub>(BO<sub>3</sub>)<sub>4</sub> crystallizes in the *P3<sub>1</sub>21* space group at both 300 and 4 K at ambient pressure conditions.<sup>41,42,44</sup> It is therefore very likely that similar behavior persists across the *P3<sub>1</sub>21* phase, including at 4 K, although of course magnetic ordering of Er and Fe (and the pressure dependence of these effect) may change this picture somewhat.

#### Revisiting Temperature Effects in Chiral ErFe<sub>3</sub>(BO<sub>3</sub>)<sub>4</sub>

Figure 6a summarizes the Raman scattering response of ErFe<sub>3</sub>(BO<sub>3</sub>)<sub>4</sub> as a function of the temperature. Ours are not the first studies of this type,<sup>16</sup> but they are the most complete, allowing us to track the systematic evolution of each phonon and establish the importance of various types of displacements across the magnetic ordering and structural phase transitions. We selected several specific features, plotted in Figures 6b–g, for a detailed analysis. The low frequency phonons involving Er motion (magenta and red symbols) display the most unusual behavior [Figure 6b]. Focusing first on the high temperature response, we see that two features near 80 cm<sup>-1</sup> have a kink at 350 K (likely due to the precursor effects) after which they harden smoothly with increasing temperature across  $T_S$  = 450 K. This rising trend is unusual. All of the other phonons display typical anharmonic behavior as well as a sharp drop across  $T_S$  as marked by the red dashed line [Figure 6c,d,f,g]. This softening occurs at slightly higher temperature than in prior reports,<sup>16</sup> probably due to superior crystal quality.

$\text{ErFe}_3(\text{BO}_3)_4$  also hosts a magnetic ordering transition  $T_N$  near 40 K<sup>11</sup> marked by the green dashed line. We observe very slight mode softening across this transition. As a reminder, the phonons in Figures 6c–e are dominated by Fe atom motion whereas those in Figure 6f,g correspond to  $\text{BO}_3$  motion. Spin is ordered below  $T_N$ , causing both Fe–O–Fe and Fe–O–B–O–Fe superexchange interactions to soften these features [Figure 6b–g]. We can quantify spin–phonon coupling by fitting frequency vs temperature data in the nonmagnetic phase with a typical anharmonic model as shown by the solid gray lines.<sup>70</sup> Given the limiting low temperature value from this fit and an estimate of the spin–spin correlation function between nearest neighbor spins, we can calculate the spin–phonon coupling constants ( $\lambda$ 's) as  $\Delta\omega = \lambda\langle S_i \cdot S_j \rangle$ .<sup>71–73</sup> The spin–phonon coupling constants that we extract from this model are less than  $\pm 0.02 \text{ cm}^{-1}$ , meaning that they are almost effectively zero. Additional discussion is given in the Supporting Information. These values are significantly smaller than those in many other heavy and mixed-metal oxides,<sup>74</sup> ruling out a substantial effect of spin–phonon coupling (at least involving the even symmetry vibrational modes) in this system.

## CONCLUSIONS

In order to explore the properties of a chiral antiferromagnet, we measured the Raman scattering and near-infrared absorbance of bimetallic  $\text{ErFe}_3(\text{BO}_3)_4$  as a function of pressure and temperature and compared our findings to first-principles calculations of the lattice dynamics and energy landscape. Overall, phonon modes involving  $\text{Er}^{3+}$  and  $\text{BO}_3^{3-}$  are robust under pressure compared to  $\text{Fe}^{2+}$ -related features. The  $\text{FeO}_6$ -related modes are the first to change under compression because the chiral chain is soft. In line with these findings, the rare earth  $^4\text{I}_{15/2} \rightarrow ^4\text{I}_{13/2}$  crystal field excitations display only small shifts in frequency under compression up to 8 GPa, suggesting that the local trigonal prismatic symmetry of  $\text{Er}^{3+}$  remains almost unchanged from that under ambient conditions. Higher pressures modify the crystal structure across a series of different space groups up to 20 GPa, although without the appearance of metallicity. We studied temperature trends in this work as well. While spin–phonon coupling is effectively zero across the  $\text{Fe}^{2+}$  ordering temperature at 40 K, the  $P3_121 \rightarrow R32$  structural phase transition near 450 K hosts a sharp and systematic softening of the  $\text{BO}_3$  and  $\text{FeO}_6$  modes as well as two  $\text{Er}^{3+}$ -containing modes with strong precursor effects that drive the system toward the higher symmetry state. Together, studies of this type have the potential to identify effective methods for achieving switchable polar and antipolar states for device and energy applications.

## ASSOCIATED CONTENT

### Supporting Information

The Supporting Information is available free of charge at <https://pubs.acs.org/doi/10.1021/acs.jpcc.Sc07666>.

Pressure calibrated using ruby fluorescence, system is reversible upon release of pressure from 20 GPa, close-up view of the structural phase transition at 3.8 GPa, no clear color change under pressure, anharmonic model fitting of the temperature effects, and first-principles calculation and analysis of Raman-active phonon modes (PDF)

## AUTHOR INFORMATION

### Corresponding Author

Janice L. Musfeldt – Department of Chemistry, University of Tennessee, Knoxville, Tennessee 37996, United States; Department of Physics and Astronomy, University of Tennessee, Knoxville, Tennessee 37996, United States;  [orcid.org/0000-0002-6241-823X](https://orcid.org/0000-0002-6241-823X); Email: [musfeldt@tennessee.edu](mailto:musfeldt@tennessee.edu)

### Authors

Yanhong Gu – Department of Chemistry, University of Tennessee, Knoxville, Tennessee 37996, United States; Present Address: State Key Laboratory of Low Dimensional Quantum Physics, Beijing Tsinghua Institute for Frontier Interdisciplinary Innovation, Beijing 102202, China

Fan Yang – Department of Chemical Engineering and Materials Science, University of Minnesota, Minneapolis, Minnesota 55455, United States

Choongjae Won – Laboratory of Pohang Emergent Materials, Department of Physics, Pohang University of Science and Technology, Pohang 37673, Korea; Max Planck POSTECH/KOREA Research Initiative, Pohang University of Science and Technology, Pohang 37673, Korea

Sang-Wook Cheong – Department of Physics and Astronomy and Keck Center for Quantum Magnetism, Rutgers University, Piscataway, New Jersey 08854, United States; Laboratory of Pohang Emergent Materials, Department of Physics, Pohang University of Science and Technology, Pohang 37673, Korea

Turan Birol – Department of Chemical Engineering and Materials Science, University of Minnesota, Minneapolis, Minnesota 55455, United States;  [orcid.org/0000-0001-5174-3320](https://orcid.org/0000-0001-5174-3320)

Complete contact information is available at: <https://pubs.acs.org/10.1021/acs.jpcc.Sc07666>

### Author Contributions

<sup>†</sup>Y.G. and F.Y. contributed equally.

### Notes

The authors declare no competing financial interest.

## ACKNOWLEDGMENTS

Research at University of Tennessee is supported by Condensed Matter Physics, Division of Materials Research at the National Science Foundation (Grant DMR-2226109). Work at Rutgers University is funded by a W. M. Keck Foundation grant to the Keck Center for Quantum Magnetism. The work at the University of Minnesota (F.Y. and T.B.) was supported by the NSF CAREER Grant DMR-2046020. Work at POSTECH was supported by the National Research Foundation of Korea (NRF) funded by the Ministry of Science and ICT (Grant RS-2022-NR068223).

## REFERENCES

- (1) Nag, A.; Butt, A. M.; Yang, M. Y.; Managutti, P. B.; Pirzada, B. M.; Mohideen, M. I. H.; Abdelhady, A. L.; Hajja, M. A.; Mohamed, S.; Merinov, B. V.; Goddard, W. A. I.; Qurashi, A. Polymorphism of  $[\text{Cu}_{15}(\text{PhCH}_2\text{CH}_2\text{S})_{13}(\text{PPh}_3)_6][\text{BF}_4]_2$  and double-helical assembly of  $[\text{Cu}_{18}\text{H}(\text{PhCH}_2\text{CH}_2\text{S})_{14}(\text{PPh}_3)_6\text{Cl}_3]$ : origin of two chiral nanoclusters with triple-helical core from intermediates. *ACS Materials Lett.* **2025**, *7*, 442–449.

- (2) Wang, G.; Qu, A.; Sun, M.; Xu, J.; Kuang, H. Chemical mechanisms and biological effects of chiral nanomaterials. *Acc. Mater. Res.* **2024**, *5*, 1221–1236.
- (3) Cheong, S.-W.; Xu, X. Magnetic chirality. *npj Quantum Mater.* **2022**, *7*, 40.
- (4) Bloom, B. P.; Paltiel, Y.; Naaman, R.; Waldeck, D. H. Chiral induced spin selectivity. *Chem. Rev.* **2024**, *124*, 1950–1991.
- (5) Inda, A.; Oiwa, R.; Hayami, S.; Yamamoto, H. M.; Kusunose, H. Quantification of chirality based on electric toroidal monopole. *J. Chem. Phys.* **2024**, *160*, 184117.
- (6) Fecher, G. H.; Kübler, J.; Felser, C. Chirality in the solid state: chiral crystal structures in chiral and achiral space groups. *Materials* **2022**, *15*, 5812.
- (7) Sun, M.-E.; Wang, Y.; Wang, F.; Feng, J.; Wang, L.; Gao, H.; Chen, G.; Gu, J.; Fu, Y.; Bu, K.; Fu, T.; Li, J.; Lu, X.; Jiang, L.; Wu, Y.; Zang, S.-Q. Chirality-dependent structural transformation in chiral 2D perovskites under high pressure. *J. Am. Chem. Soc.* **2023**, *145*, 8908–8916.
- (8) Haskel, D.; Won, C.; Joly, Y.; Strempfer, J.; Fabbris, G.; Cheong, S.-W. Deconvolution of X-ray natural and magnetic circular dichroism in chiral Dy-ferroborate. *Sci. Rep.* **2024**, *14*, 24453.
- (9) Horibe, Y.; Yang, J.; Cho, Y.-H.; Luo, X.; Kim, S. B.; Oh, Y. S.; Huang, F.-T.; Asada, T.; Tanimura, M.; Jeong, D.; Cheong, S.-W. Color theorems, chiral domain topology, and magnetic properties of  $\text{Fe}_x\text{TaS}_2$ . *J. Am. Chem. Soc.* **2014**, *136*, 8368–8373.
- (10) Yokosuk, M. O.; Kim, H.-S.; Hughey, K. D.; Kim, J.; Stier, A. V.; O'Neal, K. R.; Yang, J.; Crooker, S. A.; Haule, K.; Cheong, S.-W.; Vanderbilt, D.; Musfeldt, J. L. Nonreciprocal directional dichroism of a chiral magnet in the visible range. *npj Quantum Mater.* **2020**, *5*, 20.
- (11) Ritter, C.; Vorotynov, A.; Pankrats, A.; Petrakovskii, G.; Temerov, V.; Gudim, I.; Szymczak, R. Magnetic structure in iron borates  $\text{RFe}_3(\text{BO}_3)_4$  ( $\text{R} = \text{Er, Pr}$ ): a neutron diffraction and magnetization study. *J. Phys.: Condens. Matter* **2010**, *22*, 206002.
- (12) Golosovsky, I. V.; Mukhin, A. A.; Skumryev, V.; Ressouche, E.; Ivanov, V. Y.; Gudim, I. A. Hidden magnetic instability in the substituted multiferroics  $(\text{Nd,Tb})\text{Fe}_3(\text{BO}_3)_4$ . *Phys. Rev. B* **2024**, *109*, 014421.
- (13) Boldyrev, K. N.; Kuz'min, N. N.; Mukhin, A. A.; Ivanov, V. Y.; Dobretsova, E. A.; Popova, E. A.; Gavrilkin, S. Y.; Leonyuk, N. I.; Maltsev, V. V.; Malkin, B. Z.; Popova, M. N. Thermal and magnetic properties and optical spectroscopy of  $\text{SmCr}_3(\text{BO}_3)_4$ . *Phys. Rev. Mater.* **2021**, *5*, 104413.
- (14) Popova, M. N.; Malkin, B. Z.; Boldyrev, K. N.; Stanislavchuk, T. N.; Erofeev, D. A.; Temerov, V. L.; Gudim, I. A. Evidence for a collinear easy-plane magnetic structure of multiferroic  $\text{EuFe}_3(\text{BO}_3)_4$ : Spectroscopic and theoretical studies. *Phys. Rev. B* **2016**, *94*, 184418.
- (15) Tripathy, A.; Gautam, K.; Dey, K.; Sahu, S. R.; Ahad, A.; Upadhyay, A.; Sagdeo, A.; Francoou, S.; Bereciartua, P. J.; Gudim, I.; Strempfer, J.; Sathe, V. G.; Shukla, D. K. Structural and magnetic interplay in multiferroic  $\text{Ho}_{0.5}\text{Nd}_{0.5}\text{Fe}_3(\text{BO}_3)_4$ . *Phys. Rev. B* **2023**, *107*, 214106.
- (16) Fausti, D.; Nugroho, A. A.; van Loosdrecht, P. H.; Klimin, S. A.; Popova, M. N.; Bezmaternykh, L. N. Raman scattering from phonons and magnons in  $\text{RFe}_3(\text{BO}_3)_4$ . *Phys. Rev. B* **2006**, *74*, 024403.
- (17) Leonyuk, N. Half a century of progress in crystal growth of multifunctional  $\text{RAI}_3(\text{BO}_3)_4$  ( $\text{R} = \text{Y, Pr, Sm - Lu}$ ). *J. Cryst. Growth* **2017**, *476*, 69–77.
- (18) Pavlovskiy, M. S.; Zinenko, V. I.; Shinkorenko, A. S. Effect of a rare-earth ion on the structural instability in  $\text{RFe}_3(\text{BO}_3)_4$  crystals. *JETP Letters* **2018**, *108*, 116–120.
- (19) Oreshonkov, A. S.; Roginskii, E. M.; Shestakov, N. P.; Gudim, I. A.; Temerov, V. L.; Nemtsev, I. V.; Molokeev, M. S.; Adichtchev, S. V.; Pugachev, A. M.; Denisenko, Y. G. Structural, electronic and vibrational properties of  $\text{YAl}_3(\text{BO}_3)_4$ . *Materials* **2020**, *13*, 545.
- (20) Boldyrev, K.; Popova, M.; Bettinelli, M.; Temerov, V.; Gudim, I.; Bezmaternykh, L.; Loiseau, P.; Aka, G.; Leonyuk, N. Quality of the rare earth aluminum borate crystals for laser applications, probed by high-resolution spectroscopy of the  $\text{Yb}^{3+}$  ion. *Opt. Mater.* **2012**, *34*, 1885.
- (21) Zvezdin, A. K.; Krotov, S. S.; Kadomtseva, A. M.; Vorob'ev, G. P.; Popov, Y. F.; Pyatakov, A. P.; Bezmaternykh, L. N.; Popova, E. Magnetoelectric effects in gadolinium iron borate  $\text{GdFe}_3(\text{BO}_3)_4$ . *JETP Letters* **2005**, *81*, 272–276.
- (22) Kadomtseva, A. M.; Popov, Y. F.; Vorob'ev, G. P.; Pyatakov, A. P.; Krotov, S. S.; Kamilov, K. I.; Ivanov, V. Y.; Mukhin, A. A.; Zvezdin, A. K.; Kuz'menko, A. M.; Bezmaternykh, L. N.; Gudim, I. A.; Temerov, V. L. Magnetoelectric and magnetoelastic properties of rare-earth ferroborates. *Low Temp. Phys.* **2010**, *36*, 511–521.
- (23) Usui, T.; Tanaka, Y.; Nakajima, H.; Taguchi, M.; Chainani, A.; Oura, M.; Shin, S.; Katayama, N.; Sawa, H.; Wakabayashi, Y.; Kimura, T. Observation of quadrupole helix chirality and its domain structure in  $\text{DyFe}_3(\text{BO}_3)_4$ . *Nat. Mater.* **2014**, *13*, 611–618.
- (24) Vasiliev, A. N.; Popova, E. A. Rare-earth ferroborates  $\text{RFe}_3(\text{BO}_3)_4$ . *Low Temp. Phys.* **2006**, *32*, 735–747.
- (25) Zhang, H.; Liu, S.; Nelson, C. S.; Bezmaternykh, L. N.; Chen, Y.-S.; Wang, S. G.; Lobo, R. P. S. M.; Page, K.; Matsuda, M.; Pajerowski, D. M.; Williams, T. J.; Tyson, T. A. Structural features associated with multiferroic behavior in the  $\text{RX}_3(\text{BO}_3)_4$  system. *J. Phys.: Condens. Matter* **2019**, *31*, 505704.
- (26) Popova, M. N.; Chukalina, E. P.; Stanislavchuk, T. N.; Bezmaternykh, L. N. Different types of magnetic ordering in  $\text{RFe}_3(\text{BO}_3)_4$ ,  $\text{R} = \text{Gd, Tb, Er, and Y}$ , as studied by the method of  $\text{Er}^{3+}$  spectroscopic probe. *J. Magn. Magn. Mater.* **2006**, *300*, e440–e443.
- (27) Zvezdin, A. K.; Vorob'ev, G. P.; Kadomtseva, A. M.; Popov, Y. F.; Pyatakov, A. P.; Bezmaternykh, L. N.; Kuvardin, A.; Popova, E. A. Magnetoelectric and magnetoelastic interactions in  $\text{NdFe}_3(\text{BO}_3)_4$  multiferroics. *JETP letters* **2006**, *83*, 509–514.
- (28) Popov, Y. F.; Pyatakov, A. P.; Kadomtseva, A. M.; Vorob'ev, G. P.; Zvezdin, A. K.; Mukhin, A. A.; Ivanov, V. Y.; Gudim, I. A. Peculiarities in the magnetic, magnetoelectric, and magnetoelastic properties of  $\text{SmFe}_3(\text{BO}_3)_4$  multiferroic. *JETP* **2010**, *111*, 199–203.
- (29) Popov, Y. F.; Kadomtseva, A. M.; Vorob'ev, G. P.; Mukhin, A. A.; Ivanov, V. Y.; Kuz'menko, A.; Prokhorov, A. S.; Bezmaternykh, L. N.; Temerov, V. L. Observation of spontaneous spin reorientation in  $\text{Nd}_{1-x}\text{Dy}_x\text{Fe}_3(\text{BO}_3)_4$  ferroborates with a competitive R-Fe exchange. *JETP Letters* **2009**, *89*, 345–351.
- (30) Kadomtseva, A. M.; Vorob'ev, G.; Popov, Y. F.; Pyatakov, A.; Mukhin, A. A.; Ivanov, V. Y.; Zvezdin, A. K.; Gudim, I. A.; Temerov, V. L.; Bezmaternykh, L. N. Magnetoelectric and magnetoelastic properties of easy-plane ferroborates with a small ionic radius. *JETP* **2012**, *114*, 810–817.
- (31) Miao, M.; Sun, Y.; Zurek, E.; Lin, H. Chemistry under high pressure. *Nat. Rev. Chem.* **2020**, *4*, 508–527.
- (32) Mujica, A.; Rubio, A.; Munoz, A.; Needs, R. High-pressure phases of group-IV, III-V, and II-VI compounds. *Rev. Mod. Phys.* **2003**, *75*, 863.
- (33) Mao, H.-K.; Chen, X.-J.; Ding, Y.; Li, B.; Wang, L. Solids, liquids, and gases under high pressure. *Rev. Mod. Phys.* **2018**, *90*, 015007.
- (34) Matsuoka, T.; Kim, H.-S.; Samanta, S.; Musfeldt, J. L.; Mandrus, D. G.  $\text{MPX}_3$  van der Waals magnets under pressure ( $\text{M} = \text{Mn, Ni, V, Fe, Co, Cd}$ ;  $\text{X} = \text{S, Se}$ ). *Front. Mater. Sci.* **2024**, *11*, 1362744.
- (35) Pei, S.; Wang, Z.; Xia, J. High pressure studies of 2D materials and heterostructures: A review. *Mater. Des.* **2022**, *213*, 110363.
- (36) Coak, M. J.; Jarvis, D. M.; Hamidov, H.; Wildes, A. R.; Paddison, J. A. M.; Liu, C.; Haines, C. R. S.; Dang, N. T.; Kichanov, S. E.; Savenko, B. N.; Lee, S.; Kratochvílová, M.; Klotz, S.; Hansen, T. C.; Kozlenko, D. P.; Park, J.-G.; Saxena, S. S. Emergent magnetic phases in pressure-tuned van der Waals antiferromagnet  $\text{FePS}_3$ . *Phys. Rev. X* **2021**, *11*, 011024.
- (37) Rocquefelte, X.; Schwarz, K.; Blaha, P.; Kumar, S.; Van Den Brink, J. Room-temperature spin-spiral multiferroicity in high-pressure cupric oxide. *Nat. Commun.* **2013**, *4*, 2511.
- (38) Aoyama, T.; Yamauchi, K.; Iyama, A.; Picozzi, S.; Shimizu, K.; Kimura, T. Giant spin-driven ferroelectric polarization in  $\text{TbMnO}_3$  under high pressure. *Nat. Commun.* **2014**, *5*, 4927.

- (39) Souza-Neto, N. M.; Haskel, D.; Tseng, Y.-C.; Lapertot, G. Pressure-induced electronic mixing and enhancement of ferromagnetic ordering in  $\text{EuX}$  ( $\text{X} = \text{Te}, \text{Se}, \text{S}, \text{O}$ ) magnetic semiconductors. *Phys. Rev. Lett.* **2009**, *102*, 057206.
- (40) Lyubutin, I. S.; Gavriluk, A. G.; Andryushin, N. D.; Pavlovskiy, M. S.; Zinenko, V. I.; Lyubutina, M. V.; Troyan, I. A.; Smirnova, E. S. Pressure-induced structural transition to the polar phase in  $\text{GdFe}_3(\text{BO}_3)_4$ . *Cryst. Growth Des.* **2019**, *19*, 6935–6944.
- (41) Campá, J. A.; Cascales, C.; Gutiérrez-Puebla, E.; Monge, M. A.; Rasines, I.; Ruiz-Valero, C. Crystal structure, magnetic order, and vibrational behavior in iron rare-earth borates. *Chem. Mater.* **1997**, *9*, 237–240.
- (42) Alekseeva, O. A.; Smirnova, E. S.; Frolov, K. V.; Lyubutina, M. V.; Lyubutin, I. S.; Gudim, I. A. Crystal structure dynamics of  $\text{RFe}_3(\text{BO}_3)_4$  single crystals in the temperature range 25–500 K. *Crystals* **2022**, *12*, 1203.
- (43) Malakhovskii, A.; Sokolov, V.; Sukhachev, A.; Aleksandrovsky, A.; Gudim, I.; Molokeev, M. Spectroscopic properties and structure of the  $\text{ErFe}_3(\text{BO}_3)_4$  single crystal. *Phys. Solid State* **2014**, *56*, 2056–2063.
- (44) Hinatsu, Y.; Doi, Y.; Ito, K.; Wakeshima, M.; Alemi, A. Magnetic and calorimetric studies on rare-earth iron borates  $\text{LnFe}_3(\text{BO}_3)_4$  ( $\text{Ln} = \text{Y}, \text{La-Nd}, \text{Sm-Ho}$ ). *J. Solid State Chem.* **2003**, *172*, 438–445.
- (45) Graf, D.; Bradley, W. The crystal structure of huntite,  $\text{Mg}_3\text{Ca}(\text{CO}_3)_4$ . *Acta Crystallogr.* **1962**, *15*, 238–242.
- (46) Popova, E. A.; Vasiliev, A. N.; Temerov, V. L.; Bezmaternykh, L. N.; Tristan, N.; Klingeler, R.; Büchner, B. Magnetic and specific heat properties of  $\text{YFe}_3(\text{BO}_3)_4$  and  $\text{ErFe}_3(\text{BO}_3)_4$ . *J. Phys.: Condens. Matter* **2010**, *22*, 116006.
- (47) Boldyrev, K. N.; Malkin, B. Z.; Popova, M. N. Magnetic-field-tunable intensity transfer from optically active phonons to crystal-field excitations in the reflection spectra of the  $\text{PrFe}_3(\text{BO}_3)_4$  antiferromagnet. *Crystals* **2022**, *12*, 392.
- (48) Nelson, C. S.; Bezmaternykh, L. N.; Gudim, I. A. Temperature- and magnetic-field-tuning of magnetic phases in multiferroic  $\text{NdFe}_3(\text{BO}_3)_4$ . *JKPS* **2013**, *62*, 1410–1413.
- (49) Leonyuk, N.; Leonyuk, L. Growth and characterization of  $\text{RM}_3(\text{BO}_3)_4$  crystals. *Prog. Cryst. Growth Charact. Mater.* **1995**, *31*, 179–278.
- (50) Mao, H.; Bell, P.; Shaner, J. T.; Steinberg, D. Specific volume measurements of Cu, Mo, Pd, and Ag and calibration of the ruby R1 fluorescence pressure gauge from 0.06 to 1 Mbar. *J. Appl. Phys.* **1978**, *49*, 3276–3283.
- (51) Kohn, W.; Sham, L. J. Self-consistent equations including exchange and correlation effects. *Phys. Rev.* **1965**, *140*, A1133.
- (52) Perdew, J. P.; Burke, K.; Ernzerhof, M. Generalized gradient approximation made simple. *Phys. Rev. Lett.* **1996**, *77*, 3865–3868.
- (53) Perdew, J. P.; Ruzsinszky, A.; Csonka, G. I.; Vydrov, O. A.; Scuseria, G. E.; Constantin, L. A.; Zhou, X.; Burke, K. Restoring the density-gradient expansion for exchange in solids and surfaces. *Phys. Rev. Lett.* **2008**, *100*, 136406.
- (54) Csonka, G. I.; Perdew, J. P.; Ruzsinszky, A.; Philipsen, P. H. T.; Lebègue, S.; Paier, J.; Vydrov, O. A.; Ángyán, J. G. Assessing the performance of recent density functionals for bulk solids. *Phys. Rev. B* **2009**, *79*, 155107.
- (55) Erofeev, D.; Jablunovskis, A.; Chukalina, E. Optical spectroscopy of  $\text{ErFe}_3(\text{BO}_3)_4$ : detection of phase transitions and crystal-field levels of the  $\text{Er}^{3+}$  ground multiplet. *EPJ Web Conf.* **2018**, *185*, 07002.
- (56) Popova, M. N.; Chukalina, E. P.; Erofeev, D. S.; Jablunovskis, A.; Gudim, I. A.; Malkin, B. Z. High-resolution optical spectroscopy and modeling of spectral and magnetic properties of multiferroic  $\text{ErFe}_3(\text{BO}_3)_4$ . *Phys. Rev. B* **2020**, *101*, 205108.
- (57) De Andres, A.; Agullo-Rueda, F.; Taboada, S.; Cascales, C.; Campa, J.; Ruiz-Valero, C.; Rasines, I. Raman active phonons of  $\text{RFe}_3(\text{BO}_3)_4$  ( $\text{R} = \text{La or Nd}$ , single crystals). *J. Alloys Compd.* **1997**, *250*, 396–399.
- (58) Moshkina, E.; Krylov, A.; Sofronova, S.; Gudim, I.; Temerov, V. Crystal growth and Raman spectroscopy study of  $\text{Sm}_{1-x}\text{La}_x\text{Fe}_3(\text{BO}_3)_4$  ferroborates. *Cryst. Growth Des.* **2016**, *16*, 6915–6921.
- (59) Krylov, A. S.; Sofronova, S. N.; Gudim, I. A.; Vtyurin, A. N. Magnetoelastic interactions in Raman spectra of  $\text{Ho}_{1-x}\text{Nd}_x\text{Fe}_3(\text{BO}_3)_4$  crystals. *Solid State Commun.* **2013**, *174*, 26–29.
- (60) Clune, A.; Harms, N.; O'Neal, K. R.; Hughey, K.; Smith, K. A.; Obeysekera, D.; Haddock, J.; Dalal, N. S.; Yang, J.; Liu, Z.; Musfeldt, J. L. Developing the pressure-temperature-magnetic field phase diagram of multiferroic  $[(\text{CH}_3)_2\text{NH}_2]\text{Mn}(\text{HCOO})_3$ . *Inorg. Chem.* **2020**, *59*, 10083–10090.
- (61) Clune, A. J.; Harms, N. C.; Smith, K. A.; Tian, W.; Liu, Z.; Musfeldt, J. L. Pressure-temperature-magnetic field phase diagram of multiferroic  $(\text{NH}_4)_2\text{FeCl}_5\cdot\text{H}_2\text{O}$ . *Inorg. Chem.* **2024**, *63*, 11021–11029.
- (62) Ivantchev, S.; Kroumova, E.; Madariaga, G.; Pérez-Mato, J. M.; Aroyo, M. I. *SUBGROUPGRAPH*: a computer program for analysis of group-subgroup relations between space groups. *J. Appl. Crystallogr.* **2000**, *33*, 1190–1191.
- (63) Ivantchev, S.; Kroumova, E.; Aroyo, M. I.; Pérez-Mato, J. M.; Igartua, J. M.; Madariaga, G.; Wondratschek, H. *SUPERGROUPS* - a computer program for the determination of the supergroups of the space groups. *J. Appl. Crystallogr.* **2002**, *35*, 511–512.
- (64) Tasçi, E. S.; Elcoro, L.; Pérez-Mato, J. M.; de la Flor, G.; Aroyo, M. I. *SUBGROUPS*: a computer tool at the Bilbao Crystallographic Server for the study of pseudo-symmetric or distorted structures. *Appl. Cryst.* **2024**, *57*, 1650–1666.
- (65) Spirito, D.; Marras, S.; Martín-García, B. Lattice dynamics in chiral tellurium by linear and circularly polarized Raman spectroscopy: crystal orientation and handedness. *J. Mater. Chem. C* **2024**, *12*, 2544–2551.
- (66) Ishito, K.; Mao, H.; Kobayashi, K.; Kousaka, Y.; Togawa, Y.; Kusunose, H.; Kishine, J.-i.; Satoh, T. Chiral phonons: circularly polarized Raman spectroscopy and ab initio calculations in a chiral crystal tellurium. *Chirality* **2023**, *35*, 338–345.
- (67) The crystal structure of  $\text{KMg}_3(\text{SiO}_3)_4$  is used as a starting guess for the first principles relaxation of this structure.
- (68) Popova, M. N.; Chukalina, E. P.; Erofeev, D. S.; Jablunovskis, A.; Gudim, I. A.; Malkin, B. Z. High-resolution optical spectroscopy and modeling of spectral and magnetic properties of multiferroic  $\text{ErFe}_3(\text{BO}_3)_4$ . *Phys. Rev. B* **2020**, *101*, 205108.
- (69) Popova, E. A.; Chukalina, E. P.; Boldyrev, K. N.; Jablunovskis, A.; Gudim, I. A. Magnetic structure of  $\text{ErFe}_3(\text{BO}_3)_4$ : Spectroscopic and thermodynamic studies. *J. Magn. Magn. Mater.* **2020**, *500*, 166374.
- (70) Balkanski, M.; Wallis, R.; Haro, E. Anharmonic effects in light scattering due to optical phonons in silicon. *Phys. Rev. B* **1983**, *28*, 1928.
- (71) Lockwood, D. J.; Cottam, M. G. The spin-phonon interaction in  $\text{FeF}_2$  and  $\text{MnF}_2$  studied by Raman spectroscopy. *J. Appl. Phys.* **1988**, *64*, 5876–5878.
- (72) Suzuki, N.; Kamimura, H. Theory of spin-dependent phonon Raman scattering in magnetic crystals. *J. Phys. Soc. Jpn.* **1973**, *35*, 985–995.
- (73) Gu, Y.; Smith, K. A.; Saha, A.; De, C.; Won, C.-j.; Zhang, Y.; Lin, L.-F.; Cheong, S.-W.; Haule, K.; Ozerov, M.; Birol, T.; Homes, C.; Dagotto, E.; Musfeldt, J. L. Unconventional insulator-to-metal phase transition in  $\text{Mn}_3\text{Si}_2\text{Te}_6$ . *Nat. Commun.* **2024**, *15*, 8104.
- (74) Park, K.; Kim, J.; Choi, S.; Fan, S.; Kim, C.; Oh, D. G.; Lee, N.; Cheong, S.-W.; Kiryukhin, V.; Choi, Y. J.; Vanderbilt, D.; Lee, J. H.; Musfeldt, J. L. Spin-phonon interactions and magnetoelectric coupling in  $\text{Co}_4\text{B}_2\text{O}_9$  ( $\text{B} = \text{Nb, Ta}$ ). *Appl. Phys. Lett.* **2023**, *122*, 182902.